A fast two-step algorithm for large-area thick cloud removal in high-resolution images

Shaocong Zhu, Zhiwei Li, Huanfeng Shen & Dekun Lin

Published online: 11 Dec 2022.

Submit your article to this journal ⬀

View related articles ⬀

View Crossmark data ⬀

Taylor & Francis
Taylor & Francis Group

Check for updates

A fast two-step algorithm for large-area thick cloud removal in high-resolution images

Shaocong Zhu[a,b], Zhiwei Li[a], Huanfeng Shen [a] and Dekun Lin[a]

[a]School of Resource and Environmental Sciences, Wuhan University, Wuhan, China; [b]Hubei Luojia Laboratory, Wuhan, China

ABSTRACT

Clouds are inevitable in optical satellite images, and affect the subsequent processing and application of the images. Thick cloud removal in high-resolution imagery is challenging due to the complex spatial and radiometric variations. In this letter, we present a two-step thick cloud removal method based on fast radiometric adjustment and residual correction (FRARC), which is effective for large-area thick cloud removal in high-resolution images. Compared with other thick cloud removal methods, the proposed FRARC method achieved both satisfactory results and a high efficiency in simulated and real-data experiments. In addition, as the area covered by clouds in the imagery increases, FRARC shows a more significant improvement in efficiency compared to the other methods. The proposed FRARC method can be applied to generate cloud-free images to support seamless mapping with high-resolution images.

1. Introduction

With the rapid development of sensor technology, the acquisition of high-resolution images and multi-temporal images is now possible. However, clouds and the accompanying shadows are inevitable contaminants in high-resolution satellite images. The clouds and cloud shadows result in missing information, and thus affect the processing and precise application of satellite images. Therefore, cloud and cloud shadow removal in high-resolution satellite images is of great significance.

Thick cloud removal in satellite images is essentially a process of reconstructing the missing information (Shen et al. 2015). The thick cloud removal methods can be grouped into two main categories, according to the source of the complementary information (Li et al. 2019).

One category is the spatial-based methods which use the cloud-free areas in the images to reconstruct the cloud-contaminated areas (Lin et al. 2013). However, the spatial-based methods are not suitable for reconstructing large-area clouds under complex land cover, due to the lack of information in the cloud-contaminated areas (Zeng, Shen, and Zhang 2013). Another category is the temporal-based methods which are

---

CONTACT Huanfeng Shen ✉ shenhf@whu.edu.cn School of Resource and Environmental Sciences, Wuhan University, Wuhan, China

based on the use of complementary information from adjacent temporal images to reconstruct the cloud-contaminated areas (Xu et al. 2016). Time-series methods are common methods that are utilized for normalized difference vegetation index (NDVI) data (Jonsson and Eklundh 2002). Furthermore, many temporal-based methods are based on the use of complementary information from one or more auxiliary images to reconstruct the cloudy areas (Cheng et al. 2014), which can acquire satisfactory results if the land-cover changes are not significant between the target image and auxiliary image (Duan, Pan, and Li 2020). Recently, deep learning has been widely applied in image processing, due to its strong representation ability (Gao et al. 2020). Many data-driven deep learning frameworks have been proposed for the reconstruction of cloud-contaminated areas (Zhang et al. 2020), which can skip some of the steps of the traditional algorithms, such as the detection and segmentation of clouds (Meraner et al. 2020).

However, many thick cloud removal methods are aimed at medium- and low-resolution images, and are not suitable for use with high-resolution images. Significant radiometric differences and complex spatial details exist in high-resolution images, which result in visual disruption and the actual ground details being hard to recover. At present, there are some problems with the thick cloud removal methods for high-resolution images. Some methods can acquire a satisfactory result but have a low efficiency in removing large-area clouds. Other methods have a high efficiency but the accuracy is low.

In this letter, we propose a fast two-step algorithm for large-area thick cloud removal based on fast radiometric adjustment and residual correction (FRARC). The FRARC method can acquire high-accuracy reconstruction results with a high degree of efficiency when removing large-area thick clouds in high-resolution images.

2. Methodology

2.1. FRARC method

The inputs of the FRARC method are a target image covered by thick clouds, an auxiliary image that covers the same area as the target image, and cloud masks of the target image and auxiliary image. The cloud masks can be generated by cloud detection techniques or manual labelling. The cloud-contaminated regions in the target image can be reconstructed when the cloud-contaminated regions in the target image are cloud-free in the auxiliary image.

The FRARC method consists of two main steps. Firstly, fast radiometric adjustment based on the localized linear histogram match (LLHM) method (Scaramuzza and Barsi 2005) method is undertaken to fill the cloud-contaminated areas. Fast residual correction through global optimization is then utilized to further eliminate the radiometric inconsistencies between the recovered regions and the cloud-free areas. Figure 1 shows the flowchart of the FRARC method.

2.2. Fast radiometric adjustment

Fast radiometric adjustment based on the LLHM method is conducted on each cloud-contaminated region of the target image. For each cloud pixel in a cloud-contaminated region, the gain and bias are calculated based on the valid cloud-free pixels in local
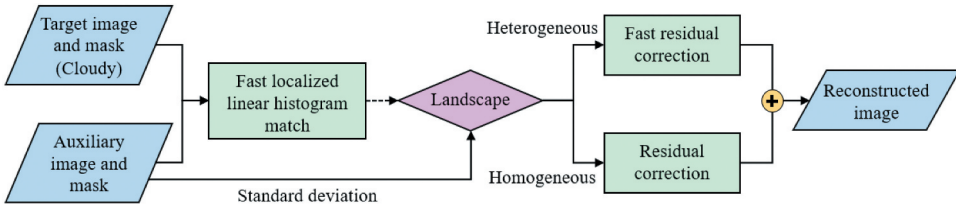
Figure 1. Flowchart of the FRARC method.

windows of the cloud-free regions of the target and auxiliary images. The recovery result for a cloud pixel in each cloud-contaminated region can be calculated as follows:

$$T'(i,j) = \frac{\sigma_T}{\sigma_R} R(i,j) + \mu_T - \frac{\sigma_T}{\sigma_R} \mu_R \tag{1}$$

where $T'(i,j)$ is the recovery result for the cloud pixel (i,j); $R(i,j)$ is the cloud-free pixel of the auxiliary image; σ_T and σ_R are the standard deviations of the valid cloud-free pixels in windows of the target and auxiliary images, respectively; μ_T and μ_R are the mean values. Noted that the standard deviations and the mean values are calculated based on the DN values of the pixels in the local window.

To accelerate the calculation of the mean and standard deviation in the local window, a box filter (Pires, Singh, and Moura 2011) is utilized in the FRARC method. In addition, to improve the efficiency and applicability of the LLHM method, the local window sizes are self-adaptive according to the cloud-contaminated region sizes, which are set to the minimum height or width of the expanded enclosing rectangle of each cloud-contaminated region. The expanded enclosing rectangle is expanded by the minimum enclosing rectangle of each cloud-contaminated region, where the expansion size is 120 pixels. The local window sizes are chosen to ensure that each pixel has enough auxiliary information, which is an approach that has better adaptability for cloud-contaminated regions of different sizes.

2.3. Fast residual correction

Due to the limitation of the LLHM method, some visual inconsistencies may exist between the recovered regions and the cloud-free areas. Therefore, fast residual correction is utilized to further eliminate the slight radiometric differences. The fast residual correction consists of two main parts.

Firstly, the FRARC method applies a standard deviation threshold based on local windows to distinguish homogeneous and heterogeneous areas, where the standard deviation is calculated based on the DN values of the near-infrared (NIR) or red band of the auxiliary image. Empirically, the local window radius for computing the standard deviation is set to 5, and the standard deviation threshold used to distinguish homogeneous and heterogeneous areas is set to 0.025 in 2-m resolution images.

Secondly, the FRARC method uses residual correction to further eliminate the radiation differences (Pérez, Gangnet, and Blake 2003), where the FRARC method refers to the method of residual correction in the stepwise radiometric adjustment and residual correction (SRARC) method (Li et al. 2019). The result of the adjusted image after residual
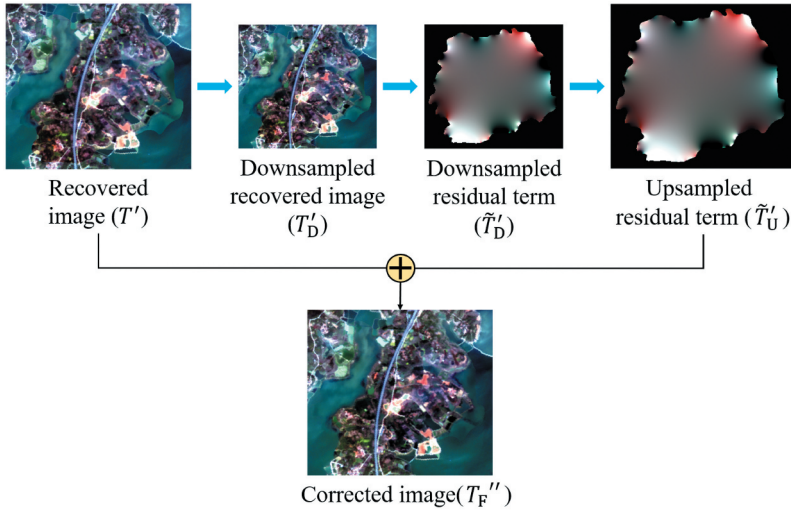
Figure 2. The process of fast residual correction.

correction (T'') and the residual term ($\tilde{T}'$) can be calculated according to Equations (2) and (3), respectively:

$$T'' = T' + \tilde{T}' \tag{2}$$

$$\tilde{T}' = \arg\min \iint_{\Omega} (|\nabla \tilde{T}'|^2 + \lambda |\tilde{T}'|^2) \tag{3}$$

where Ω is the corrected region; T' is the recovered image produced by radiometric adjustment; ∇ is the gradient operator; and λ is the weight used to balance the fidelity of the gradient and intensity.

For heterogeneous areas, to reduce the huge calculation cost of residual correction, fast residual correction is undertaken, which can achieve a high efficiency at the loss of some accuracy. Empirically, the residual term in both heterogeneous and homogeneous areas is smooth, and the loss of accuracy is slight when performing downsampling or upsampling to a smooth image. Therefore, in the fast residual correction, a downsampled residual term ($\tilde{T}'_D$) can be generated by applying the residual correction to a downsampled recovered image (T'_D). Upsampling is then performed for the downsampled residual term ($\tilde{T}'_D$) to generate the upsampled residual term ($\tilde{T}'_U$). The result of the adjusted image after fast residual correction (T_F'') can be calculated by the recovered image (T') and the upsampled residual term ($\tilde{T}'_U$). Figure 2 shows the process of fast residual correction.

Due to the homogeneous areas being sensitive to radiometric inconsistencies, slight visual inconsistencies may still exist if the fast residual correction is utilized in homogeneous areas. Generally, the homogeneous areas that need to be corrected are relatively small. Therefore, the residual correction is utilized to eliminate the visual disruption in homogeneous areas.

3. Experimental results and analysis

3.1. Experimental design

We tested the FRARC method in both simulated-data and real-data experiments. The experimental data were Beijing-2 Panchromatic and Multi-Spectral (PMS) images with a 4-m resolution, and Gaofen-1 PMS images with a 2-m spatial resolution, which were obtained by panchromatic and multispectral image fusion. The experiments were performed on the fused multispectral images. The compared methods were the LLHM (Scaramuzza and Barsi 2005), the modified neighbourhood similar pixel interpolator (MNSPI) (Zhu et al. 2012), and the SRARC (Li et al. 2019). All these methods need auxiliary images to reconstruct the cloud-contaminated areas in the target image, and only the SRARC and FRARC methods can remove large-area clouds in high-resolution images effectively. Note that the first simulated-data experiment was conducted on a desktop computer (Windows system, Intel Core i7–10700 CPU, 32-GB RAM), while the second simulated experiment and the real-data experiment were conducted on a workstation (Linux system, Intel Xeon Gold 6248 R CPU, 250-GB RAM), due to the requirements of large-size image processing.

3.2. Simulated-data experiments

In the simulated-data experiments, the clouds extracted from other images were applied to the cloud-free images as the target images, and the cloud-free images were considered to be the ground truth in the accuracy evaluation. The metrics used for the accuracy evaluation in this letter are the correlation coefficient (CC), the root-mean-square error (RMSE), the universal image quality index (UIQI) (Wang and Bovik 2002), and the time consumption (Time). Note that the UIQI can be used to evaluate the spatial structure similarity between the reconstructed image and the ground truth in areas where cloud has been removed, and the metrics were calculated based on the recovered cloud-contaminated areas. Table 1 lists the quantitative evaluation results for the two simulated experiments, and Figures 3 and 4 show the results of the simulated experiments. Note that the window size of the LLHM method in the experiments was set to 117 pixels, referring to the image resolution and the corresponding window size setting in the original paper (Scaramuzza and Barsi 2005). In addition, the MNSPI method was from a publicly available tool released by the authors of the original paper (Zhu et al. 2012), and the images were processed entirely, instead of block by block, to ensure that the MNSPI

Table 1. Quantitative evaluation results for the simulated cloud removal experiments. The up arrow means the higher the value the better the result, the down arrow is opposite.

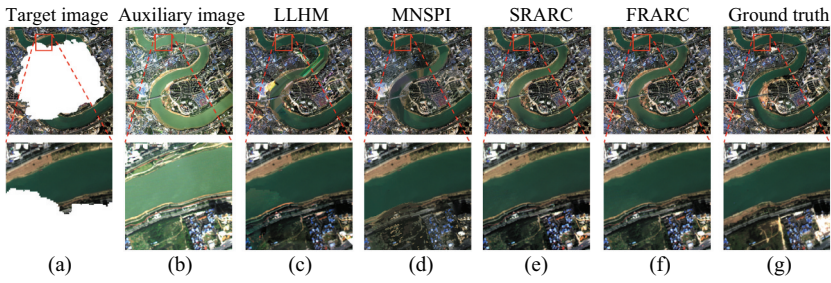|	Method	CC (↑)	RMSE (↓)	UIQI (↑)	Time (s)
Scene 1	LLHM	0.604	0.082	0.597	17436
(1000×1000×4)	MNSPI	0.410	0.198	0.365	18906
	SRARC	0.755	0.055	0.754	41
	FRARC	0.753	0.054	0.753	15
Scene 2	LLHM	N/A	N/A	N/A	N/A
(21512×18936×4)	MNSPI	N/A	N/A	N/A	N/A
	SRARC	0.921	0.027	0.919	33068
	FRARC	0.907	0.028	0.906	5243

Figure 3. The first simulated experiment on 4-m resolution Beijing-2 PMS images with a size of 1000 × 1000 × 4. (a) Target image. (b) Auxiliary image. (c)–(f) Cloud removal results of LLHM, MNSPI, SRARC, and FRARC, respectively. (g) Ground truth.

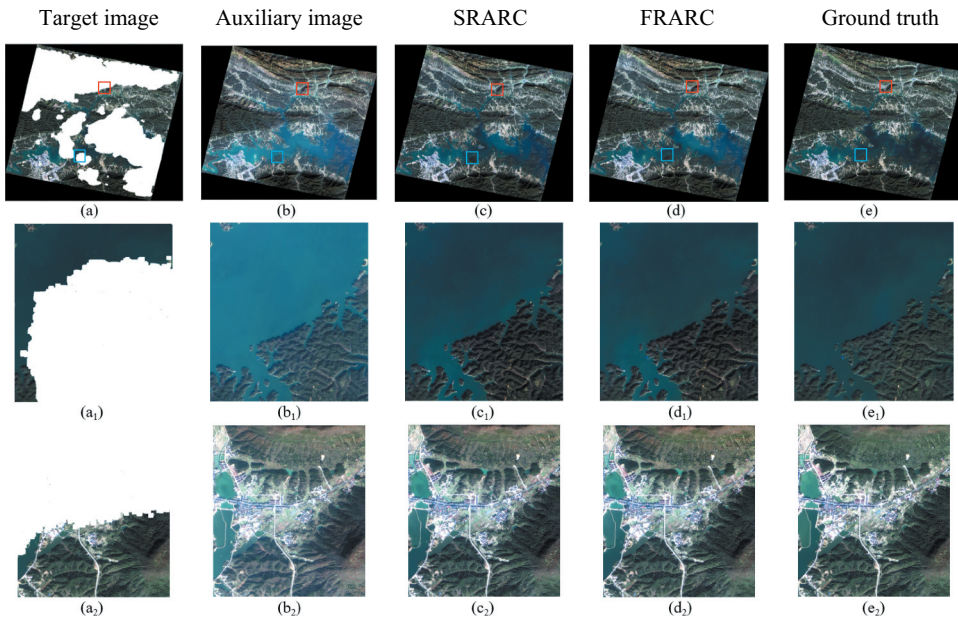**Figure 4.** The second simulated experiment on 2-m resolution Gaofen-1 PMS images with a size of 21,512 × 18936 × 4. (a) Target image. (b) Auxiliary image. (c)–(d) Cloud removal results of SRARC and FRARC, respectively. (e) Ground truth. (a_1)–(e_1) and (a_2)–(e_2) Zoomed images of areas marked in blue and red, respectively. .

method could obtain the best possible results. Since both the LLHM and MNSPI methods cannot generate results on a Linux system workstation, which was selected to perform cloud removal for the extremely large-size images in the second simulated experiment, the LLHM and MNSPI methods were not applied in the second simulated-data experiment.

In the first simulated-data experiment (Figure 3), 4-m resolution Beijing-2 PMS images with a size of 1000-pixel width, 1000-pixel height and 4 bands and 83.8% thick cloud cover were utilized as the experimental images. The target and auxiliary images were acquired in October 2017 and October 2016, respectively, and are located at 108.3° E and 22.8° N. From

the results shown in Figure 3, it can be seen that the result of LLHM has some colour distortion in the recovered areas, and the result of MNSPI is affected by the produced noise and artefacts. The results of SRARC and FRARC show good spatio-spectral consistency. As can be seen in Table 1, FRARC obtains a higher CC (0.753) and UIQI (0.753) than LLHM and MNSPI, and performs similarly to SRARC. However, FRARC requires much less time consumption (15 s) than the other methods. Overall, the results show that FRARC can obtain a high degree of efficiency while maintaining an accuracy that is as high as that of SRARC.

In the second simulated-data experiment (Figure 4), 2-m resolution Gaofen-1 PMS images with a size of 21,512-pixel width, 18936-pixel height and 4 bands and extremely thick cloud cover of 50.3% were utilized as the experimental images. The target and auxiliary images were acquired in November 2020 and December 2020, respectively. The images are located at 115.2° E and 29.4° N and cover both homogeneous and heterogeneous landscapes. It can be seen from the results shown in Figure 4 that both SRARC and FRARC maintain a good spatio-spectral consistency, and the quantitative evaluations of the two methods are close. Due to the slight land-cover changes that occurred between the two images, SRARC and FRARC both acquire a high quantitative evaluation accuracy, as shown in Table 1. However, FRARC costs less time (5243 s) than SRARC (33068 s), which shows that FRARC is more efficient than SRARC.

3.3. Real-data experiment

The real-data experiment was conducted on Gaofen-1 PMS images with a 2-m resolution. The images were acquired in August and October of 2020, with 11.8% and 31.1% cloud cover, respectively. The images are located at 115.2° E and 30.5° N and the overlap area between the two images is 20,935-pixel width, 15632-pixel height and 4 bands. In this case, the images were reconstructed based on the complementary information in each image. As shown in Figure 5, SRARC and FRARC can remove the clouds and cloud shadows, and the results are seamless. Although the result generated by FRARC shows slight radiometric differences between the cloud-free and recovered areas, both FRARC and SRARC acquire visually satisfactory results. In addition, FRARC (1659 s and 2541 s) consumed much less time than SRARC (8900 s and 10,997 s) in the real-data experiment, which suggests that FRARC is more efficient in removing large-area clouds in high-resolution images.

The results of the first simulated-data experiment showed that the results of the LLHM method usually contain significant radiometric inconsistencies and colour distortion, and the results of the MNSPI method are easily affected by noise, which was also observed in our previous study (Li et al. 2019). The results of both the simulated and real-data experiments conducted in this study showed that the SRARC method can achieve a good performance but the efficiency is low in removing large-area clouds. In comparison, the FRARC method can obtain high-accuracy reconstruction results with a high degree of efficiency, and can also keep the radiometric consistency and spatial details in different landscapes.
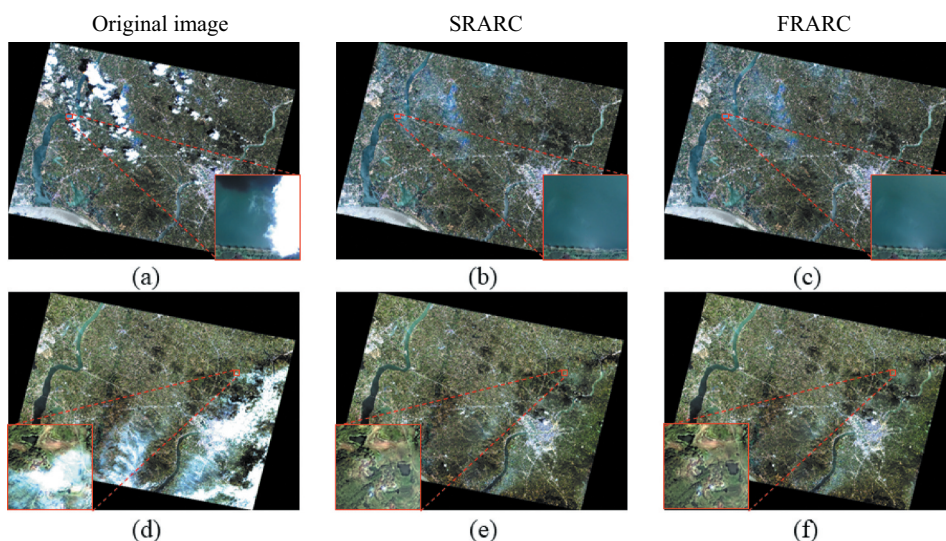
Original image   SRARC   FRARC

Figure 5. The real-data experiment with Gaofen-1 PMS images with a 2-m resolution. (a) Image acquired in August 2020. (b)–(c) Cloud removal results of SRARC and FRARC, respectively. (d) Image acquired in October 2020. (c)–(f) Cloud removal results of SRARC and FRARC, respectively.

4. Discussion and conclusion

In this letter, we have described how we developed the FRARC method for large-area thick clouds removal in high-resolution images. Compared with the other thick cloud removal methods, the proposed method shows a significant efficiency improvement, of over 60%, and with the increase of the cloud-covered area, the efficiency can be increased by more than 80%. The FRARC method contains two main steps. Firstly, LLHM is used to fill the cloud-contaminated areas, in which a box filter and localized self-adaptive window sizes are used to improve the efficiency. Secondly, the FRARC method applies a standard deviation threshold to distinguish between homogeneous and heterogeneous areas. For the heterogeneous areas, FRARC utilizes fast residual correction to eliminate the slight visual inconsistency which can reduce the huge calculation required for residual correction. For the homogeneous areas, residual correction is undertaken to eliminate the radiometric differences with a high degree of accuracy. In the future, the proposed thick cloud removal method will be applied to generate high-resolution seamless maps of the areas of interest.

Disclosure statement

No potential conflict of interest was reported by the author(s).

Funding

ORCID

Huanfeng Shen 🔾 http://orcid.org/0000-0002-4140-1869

References

Cheng, Q., H. Shen, L. Zhang, Q. Yuan, and C. Zeng. 2014. "Cloud Removal for Remotely Sensed Images by Similar Pixel Replacement Guided with a Spatio-Temporal MRF Model." *Isprs Journal of Photogrammetry and Remote Sensing* 92: 54–68. doi:10.1016/j.isprsjprs.2014.02.015.

Duan, C., J. Pan, and R. Li. 2020. "Thick Cloud Removal of Remote Sensing Images Using Temporal Smoothness and Sparsity Regularized Tensor Optimization." *Remote Sensing* 12 (20): 3446. doi:10.3390/rs12203446.

Gao, J., Q. Yuan, J. Li, H. Zhang, and X. Su. 2020. "Cloud Removal with Fusion of High Resolution Optical and SAR Images Using Generative Adversarial Networks." *Remote Sensing* 12 (1): 191. doi:10.3390/rs12010191.

Jonsson, P., and L. Eklundh. 2002. "Seasonality Extraction by Function Fitting to Time-Series of Satellite Sensor Data." *IEEE Transactions on Geoscience and Remote Sensing* 40 (8): 1824–1832. doi:10.1109/TGRS.2002.802519.

Li, Z., H. Shen, Q. Cheng, W. Li, and L. Zhang. 2019. "Thick Cloud Removal in High-Resolution Satellite Images Using Stepwise Radiometric Adjustment and Residual Correction." *Remote Sensing* 11 (16): 1925. doi:10.3390/rs11161925.

Lin, C. H., P. H. Tsai, K. H. Lai, and J. Y. Chen. 2013. "Cloud Removal from Multitemporal Satellite Images Using Information Cloning." *IEEE Transactions on Geoscience and Remote Sensing* 51 (1): 232–241. doi:10.1109/TGRS.2012.2197682.

Meraner, A., P. Ebel, X. X. Zhu, and M. Schmitt. 2020. "Cloud Removal in Sentinel-2 Imagery Using a Deep Residual Neural Network and SAR-Optical Data Fusion." *Isprs Journal of Photogrammetry and Remote Sensing* 166: 333–346. doi:10.1016/j.isprsjprs.2020.05.013.

Pérez, P., M. Gangnet, and A. Blake. 2003. "Poisson Image Editing." *ACM Transactions on Graphics* 22 (3): 313–318. doi:10.1145/882262.882269.

Pires, B. R., K. Singh, and J. M. Moura 2011. "Approximating Image Filters with Box Filters." 2011 18th IEEE International Conference on Image Processing. 85–88. doi: 10.1109/ICIP.2011.6116693.

Scaramuzza, P., and J. Barsi. 2005. "Landsat 7 Scan Line Corrector-Off Gap-Filled Product Development." *Proceeding of Pecora* 16: 23–27.

Shen, H., X. Li, Q. Cheng, C. Zeng, G. Yang, H. Li, and L. Zhang. 2015. "Missing Information Reconstruction of Remote Sensing Data: A Technical Review." *IEEE Geoscience and Remote Sensing Magazine* 3 (3): 61–85. doi:10.1109/MGRS.2015.2441912.

Wang, Z., and A. C. Bovik. 2002. "A Universal Image Quality Index." *IEEE signal processing letters* 9 (3): 81–84. doi:10.1109/97.995823.

Xu, M., X. Jia, M. Pickering, and A. J. Plaza. 2016. "Cloud Removal Based on Sparse Representation via Multitemporal Dictionary Learning." *IEEE Transactions on Geoscience and Remote Sensing* 54 (5): 2998–3006. doi:10.1109/TGRS.2015.2509860.

Zeng, C., H. Shen, and L. Zhang. 2013. "Recovering Missing Pixels for Landsat ETM+ SLC-Off Imagery Using Multi-Temporal Regression Analysis and a Regularization Method." *Remote sensing of environment* 131: 182–194. doi:10.1016/j.rse.2012.12.012.

Zhang, Q., Q. Yuan, J. Li, Z. Li, H. Shen, and L. Zhang. 2020. "Thick Cloud and Cloud Shadow Removal in Multitemporal Imagery Using Progressively Spatio-Temporal Patch Group Deep Learning." *Isprs Journal of Photogrammetry and Remote Sensing* 162: 148–160. doi:10.1016/j.isprsjprs.2020.02.008.

Zhu, X., F. Gao, D. Liu, and J. Chen. 2012. "A Modified Neighborhood Similar Pixel Interpolator Approach for Removing Thick Clouds in Landsat Images." *IEEE Geoscience and Remote Sensing Letters* 9 (3): 521–525. doi:10.1109/LGRS.2011.2173290.